This is the accepted manuscript made available via CHORUS. The article has been published as:

Anisotropic temperature distribution in carbon nanotube bundles determined using two types of phase transitions of nanoparticles

Hiromu Hamasaki, Takumi Kawase, and Kaori Hirahara

Phys. Rev. Materials **6**, L023001 — Published 16 February 2022

DOI: 10.1103/PhysRevMaterials.6.L023001

Anisotropic temperature distribution in carbon nanotube bundles determined using two types of phase transitions of nanoparticles

Hiromu Hamasaki[a]*, Takumi Kawase*[a] *and Kaori Hirahara*[b]

[a]Department of Mechanical Engineering, Osaka University, 2-1 Yamadaoka, Suita, Osaka, 565-0871, Japan

[b]Department of Mechanical Engineering and Center for Atomic and Molecular Technologies, Osaka University, 2-1 Yamadaoka, Suita, Osaka, 565-0871, Japan

KEYWORDS: carbon nanotubes, thermal transport, anisotropic materials, van der Waals materials

The boundary between carbon nanotubes is an important factor affecting the transport properties of carbon-nanotube-based materials. Recently, carbon nanotube bundles have been shown to have very high thermal anisotropy due to boundaries at 1,000 °C. However, it is unclear whether the anisotropy is peculiar to this high-temperature region. Here, we conduct an in-situ study of the anisotropic thermal properties of bundles of carbon nanotubes by utilizing the phase transition of Sn nanoparticles. The results indicate that the anisotropic thermal properties are not unique to

1,000 °C. Moreover, observation of two different phase transitions of Sn particles enables the direct comparison of two temperature regions and indicates that carbon nanotube bundles have higher anisotropy at lower temperatures. A simple finite element calculation suggests that the size-dependent thermal conductivity of carbon nanotube bundles can be attributed to the extremely large anisotropy estimated in this study.

Carbon nanotubes (CNTs) have drawn considerable attention due to their extraordinary potential for thermal management devices. Individual CNTs exhibit thermal conductivity that is one order of magnitude higher than that of highly thermal conductive metals, such as copper[1-3]. However, discrepancies between the thermal conductivities of individual CNTs (~10^3 $Wm^{-1}K^{-1}$), CNT bundles (~10^2 $Wm^{-1}K^{-1}$)[3-5], and macroscopic bulk aggregates (<10^2 $Wm^{-1}K^{-1}$)[6-9] have been experimentally demonstrated. One of the main differences between a single CNT and CNT assemblies is the existence of boundaries between CNTs, which may result in the discrepancies mentioned above. To elucidate the effect of these boundaries, several theoretical[10-14] and experimental[6-9,15] studies have been conducted mainly at microscopic and macroscopic scales, respectively. Further understanding of the thermal behavior at the mesoscopic scale can allow us to relate single-CNT-level microscopic properties to macroscopic behavior.

Recently, thermal transport in bundles of single-walled carbon nanotubes (SWCNTs) has been experimentally investigated by in situ observation of the evaporation of gold (Au) nanoparticles decorated on the bundles as thermomarkers by transmission electron microscopy (TEM)[16]. The bundle of SWCNTs was revealed to exhibit large anisotropy of thermal conductivity due to the boundaries between CNTs, and the anisotropy was, for the most part, larger than that of macroscopically aligned SWCNT specimens[6-9]. However, because particle evaporation of Au is

utilized, this method is not appropriate at temperatures below ~1,000 °C, and it is unclear whether the large anisotropy is an inherent property of CNTs or is unique to high temperatures around the melting point of Au. The use of evaporation of an alternative metal may be considered for such experiments at lower temperatures; however, this approach is less useful, as low-melting-point metals are generally oxidized at the surface, which prevents evaporation of the thermomarkers at the melting point.

In this study, we employ the method of temperature mapping using dark-field TEM proposed by Brintlunger et al,[17] who utilized the phase transition of indium (In) particles (>60 nm diameter) as a thermomarker by monitoring changes in the dark-field image intensity from the solid to the liquid state. This method makes it possible to observe the temperature distributions in a relatively low-temperature region (~150 °C). In this study, tin (Sn) nanoparticles were selected as thermomarkers. This is because the melting point of Sn nanoparticles has been well studied in terms of its size dependency[18,19]. Observations of Sn melting revealed that SWCNT bundles have highly anisotropic thermal conductivities even around 200 °C. Moreover, the use of melting in combination with evaporation made it possible to observe the phenomena at two different temperature regions of the same bundle. A comparison between the temperature distributions of the melting and evaporation temperatures of Sn nanoparticles was performed to investigate the temperature dependence of anisotropy. In addition, the experimental discrepancy between the thermal conductivities of individual CNTs and CNT bundles is discussed on the basis of a simple finite element calculation according to the extremely high anisotropy estimated in this study.

Sn nanoparticles were decorated by vacuum vapor deposition on a surface of SWCNT specimen (Meijo Nano Carbon Co., ARC SO) supported on a half-cut microgrid, which is the standard supporting medium for TEM observation. The schematic in Fig. 1a displays the

experimental setup used for in situ thermal transport observation in TEM. The tip of a conductive cantilevered probe (NSC36, Mikro Masch) was brought into contact with the bundle of SWCNTs projecting from the edge of the half-cut microgrid by controlling the manipulator. Subsequently, Joule heat was generated by applying an electric current to the bundle between the probe tip and substrate, which was controlled by a digital multimeter (Keithley 2612A). Here, the two-terminal electrical resistance measured by the digital multimeter (see Supplemental Material[20]) was typically two orders of magnitude higher than that of the SWCNT bundle calculated based on the reported value (for specimens generated by the pulsed laser ablation method)[5]. This suggests that the measured electrical resistance could be mainly attributed to the contact resistance, particularly the contact between the bundle and cantilever, which likely made point contact with the smallest contact area in the system. Therefore, the contact point was likely the main heat source in this experiment. The generated Joule heat flowed into the bundle, and a greater amount of heat was supplied to the bundle by increasing the applied electric current. The temperature distribution occurring on the bundle was obtained by monitoring the melting of Sn nanoparticles by utilizing the dark-field imaging mode of TEM. Note that the stable observation of liquid-state Sn particles in vacuo was achieved by the presence of natural oxide layers on their surface, preventing evaporation above the melting point.

Figure 1b presents a bright-field TEM image of a bundle of SWCNTs decorated with Sn nanoparticles at room temperature. It can be seen that the electrode tip was attached to the bundle at the lower edge. In addition, the left side of the bundle was connected to the substrate, and the right side was the free-standing end. In this geometrical setup, heat flowed independently of the electric current on the right side from the electrode tip contact. Figure 1c presents a dark-field image taken of the same portion of the specimen as the bright-field image in Fig. 1b. The objective

aperture was placed where both diffraction patterns of solid and liquid states of Sn were partially included (see Supplemental Material[20]). In this configuration, solid Sn nanoparticles exhibited two different image intensities depending on whether the diffraction spots originating from each particle appeared outside or inside the aperture. For example, particles A and B in Fig. 1c correspond to the former and latter cases, respectively, showing negligibly weak and remarkably strong contrast. When the particles turned into liquid at high temperature, diffraction originating from each particle became a halo-like diffused ring and was always partially included in the aperture. Therefore, all liquid particles uniformly exhibited medium intensity (e.g., particle A´ in Fig. 1d). Focusing on the distribution of particles exhibiting medium contrast on the bundle in Fig. 1d, the Sn particles melted preferentially along the alignment direction of the CNTs, similar to the schematic in Fig. 1a.

Herein, we utilized particles with a specific size range found on the SWCNT bundle for the semiquantitative estimation of the anisotropy ratio. We found Sn particles with diameters of 23–27 nm on the bundle illustrated in Figs. 1e and f, and the melting point of the Sn particles in this size range was approximately 208 °C–220 °C including the error bars, according to a previous study[19]. Figure 1e presents a subtracted image of two dark-field images taken from the same region when the applied electric current was 11.9 and 12.0 μA to detect the changing image contrast due to the particles. These particles can be seen as bright dots, as indicated by red arrows in Fig. 1e (particles with 23–27 nm in diameter were chosen), revealing the melting particles by increasing the applied electric current from 11.9 to 12.0 μA (power output changed from 33.8 to 34.0 μW). The corresponding melting particles are also marked by red circles in the bright-field image presented in Fig. 1f. When adjacent non-melting particles are marked by yellow circles, the

temperature contour at 214 (±6) °C should be placed between the particles marked by red and yellow circles.

The results reveal a highly anisotropic temperature contour. The anisotropy ratio of thermal conductivity of the SWCNT bundle was estimated by comparing the experimentally obtained temperature contours with simulated contours by finite element calculation using COMSOL Multiphysics software (ver. 5.6). Figure 1g presents a continuum model for the calculation based on the actual bundle size. The ratio of thermal conductivity along the z-axis (κ_z) to that along the xy-axis ($\kappa_{x,y}$), denoted by $\kappa_z/\kappa_{x,y}$, is defined as the anisotropy ratio, which corresponds to the ratio of the thermal conductivity in the alignment direction of the SWCNT bundle to that in the perpendicular directions of the SWCNT bundle. Temperature contours were generated on this model due to the temperature difference between the heat source and heat sink, and displayed anisotropic spread depending on the anisotropy ratio $\kappa_z/\kappa_{x,y}$. Plausible values are assigned for some of the model parameters, such as the power of heat source and temperature of the heat sink, however, their absolute values are not reflected in the anisotropic spread of the contour lines (see Supplemental Material[20]). Three calculated temperature contours are presented in Fig. 1h for $\kappa_z/\kappa_{x,y}$ of 10, 100, and 500. The coordinates of the melting and non-melting particles on the bundle are also plotted on the same schematic. Good agreement between the experimentally observed and computationally predicted temperature contours is seen at $\kappa_z/\kappa_{x,y} = 500$, similar to the case at 1,000 °C[16]. Note that all simulated contours were not in perfect agreement with the experimental results, likely because the calculation model did not duplicate the exact structure of the actual bundle. For example, as illustrated in Fig. 2b, the edge of the bundle was slightly wavy. This suggests that the highly thermal conductive direction in the bundle should also be wavy, unlike in the calculation model.

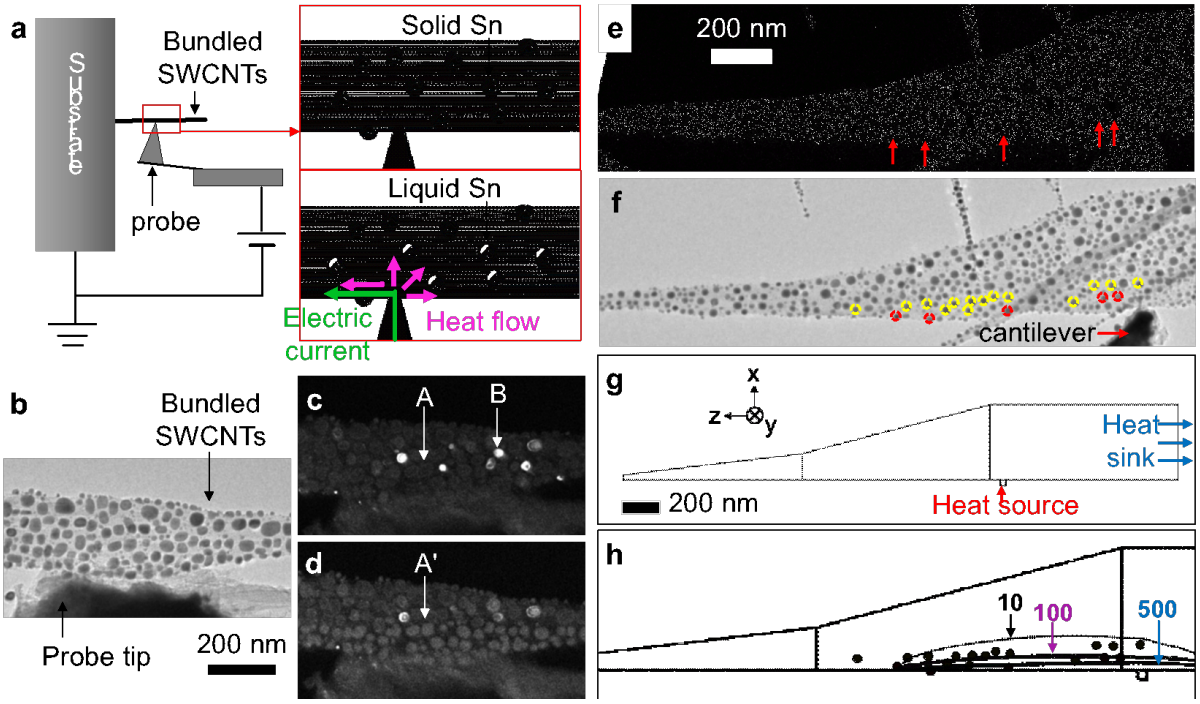


Figure 1. Visualization of anisotropic temperature distribution of bundles of single-walled carbon nanotubes (SWCNTs) by monitoring the melting of Sn nanoparticles. (a) Schematic of the experimental setup. Joule heat is generated by electric current flowing through the circuit. (b) Bright-field transmission electron microscopy (TEM) image of a tin (Sn)-decorated bundle in contact with the probe tip. Black particles on the bundle are the Sn nanoparticles. (c) Dark-field image of the same region as (b). Both particles A and B are solid Sn particles exhibiting two different intensities. (d) Dark-field image of the bundle when electric current flows. Particle A´ is a liquid Sn particle. (e) Subtracted dark-field TEM image of the bundle during Joule heating, extracting the melting nanoparticles when the electric current is increased from 11.9 to 12.0 μA, as indicated by red arrows. (f) Corresponding bright-field image. The melting particles and neighboring non-melting particles with diameters of 23–27 nm are indicated by red and yellow circles, respectively. (g) Simple continuum model based on the actual size of the bundle for finite element analysis. (h) Calculated temperature contours (solid lines) when the anisotropy ratio $\kappa_z/\kappa_{x,y}$ is 10, 100, and 500. The positions of melting and non-melting particles drawn in (f) are overlapped for comparison.

Both the experimental and computational studies described above suggested that the bundle of SWCNTs had similar anisotropy ratios at 200 °C and 1,000 °C[16]. However, the semiquantitative analysis performed above did not provide the magnitude relation of the anisotropy ratio between two cases when the difference of anisotropy ratio was small. Here, we considered the use of evaporation of individual Sn nanoparticles as another thermomarker for a higher temperature range, and a comparison between two different temperature regions was performed by utilizing the same particles on the bundle. With a further increase in the temperature above the melting point of the Sn nanoparticles, liquid Sn nanoparticles started evaporating by breaking their surface oxide layer. The evaporating temperature was 800 °C–850 °C in the case of 20-nm diameter Sn nanoparticles (see Supplemental Material[20]). By monitoring the two different phase transitions of Sn nanoparticles (i.e., phase transition from solid to liquid and from liquid to gas), we were able to directly compare the anisotropy ratio at two different temperature regions of a single specimen.

Figure 2a presents dark- and bright-field TEM images of the bundle at room temperature. First, melting of the individual Sn nanoparticles by increasing the electric current was observed by the dark-field imaging mode, as illustrated in Figs. 2b and c. The electric current and power output were 17.8 μA and 47.6 μW, respectively, in Fig. 2b, and 18.8 μA and 50.2 μW, respectively, in Fig. 2c. We observed particles melting preferentially along the alignment direction. Then, the evaporation of these particles around 800 °C was tracked in the bright-field images, as illustrated in Figs. 2d and e by further increasing the electric current. The electric current and power output were 167 μA and 438 μW, respectively, in Fig. 2d, and 176 μA and 461 μW, respectively, in Fig. 2e. The image in Fig. 2d (or 2b) was taken at the moment when particle D in Fig. 2a completely evaporated (or melted). The positions of the vanished particles with diameters of 22–25 nm are

indicated by red circles in Fig. 2d. The corresponding particles in Fig. 2b are indicated by red or yellow circles when they are liquid or solid, respectively. We can see that the temperature distribution at ~800 °C spread more widely in the direction perpendicular to the alignment than the temperature distribution at ~200 °C. The same tendency can be observed by comparing Figs. 2c and e (in these images, particles with diameters of 18–20 nm are focused on to track the selective temperature range). This can be explained by the difference in phonon density of states of inter and intra SWCNTs. Hone *et al*. experimentally investigated the temperature-dependent specific heat of SWCNTs bundles and found that the specific heat of the bundle is in excellent agreement with model calculation of individual SWCNT above 8 K, implying low Debye temperature along inter-tube direction[21]. Also, Rols *et al*. investigated phonon density of state of SWCNTs bundles by inelastic neutron scattering experiment and showed that the phonon associated with bundle lattice appears only around low-frequency region below 10 meV[22]. A previous study on atomistic Green function calculation also suggested that thermal transport by high-frequency phonons is strongly suppressed along the inter-tube direction[12]. The calculation in that study resulted in a large thermal resistivity of dense SWCNTs pellet, which is 600 times larger than that of isolated SWCNTs (comparable to the estimation in this study). Thermal transport by such low-frequency phonons would lead to a weaker temperature dependence of thermal conductivity above room temperature along the inter-tube direction because of the suppression of Umklapp scattering, compared to the transport along the intra-tube direction[2]; therefore, the anisotropy ratio of bundled SWCNTs is expected to decrease with an increase in temperature above room temperature. The temperature dependence of the anisotropy ratio experimentally investigated in this study is consistent with the speculation above.

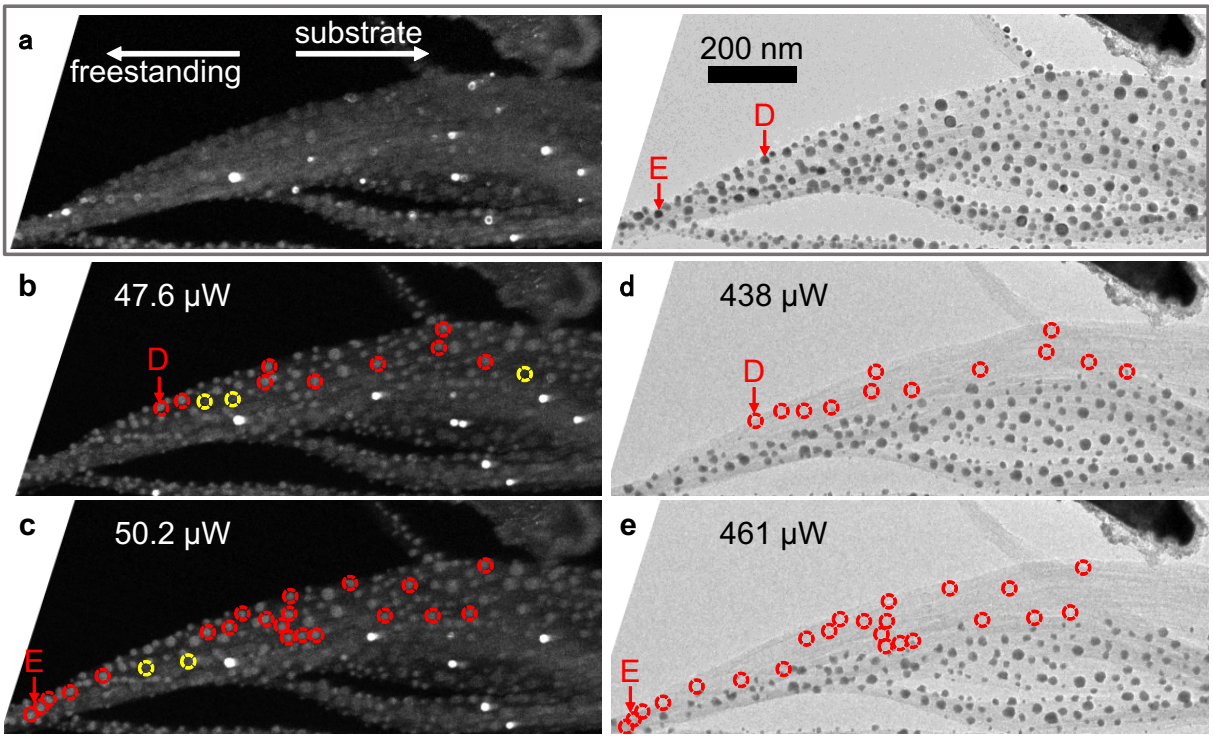


Figure 2. Transmission electron microscopy images of a Sn-decorated single-walled carbon nanotube bundle during the melting (~200 °C) and evaporation (~800 °C) process of Sn nanoparticles by Joule heating. (a) Dark-field (left) and bright-field (right) images at room temperature. (b), (c) Changing dark-field image contrasts of Sn particles due to melting. (d), (e) Bright-field images when particles D and E evaporate, respectively. The positions of the evaporated particles with specific sizes are indicated by red circles (focusing on particles whose diameters are 22–25 nm in (d) and 18–20 nm in (e)). The corresponding particles in (d) and (e) are also marked in dark-field images in (b) and (c), where red and yellow circles correspond to melting (solid state) and not melting (liquid state), respectively.

The experimental results and discussion above imply that the bundle of SWCNTs has extremely high anisotropic thermal conductivity even at room temperature, similar to that at 200 °C and 800 °C. This high anisotropy may strongly affect the measurement of the thermal

conductivity of the bundle. In most measurements of the thermal conductivity of individual bundles[3-5], the bundles were suspended on two membranes produced by microfabrication technology. Here, we consider the contact morphology for such a bridged bundle. In those experiments, two edges of the bundle were set *on* the membranes, not *between*. Namely, not the ends of the individual SWCNTs constituting the bundle, but the sidewalls of only a limited number of SWCNTs at the bundle surface, made contact with the membrane. Therefore, the temperature gradients in the bundle should be generated along not only the axial direction but also the radial direction of the bundle, as visualized in this study, which is due to the extremely high anisotropy of the thermal conductivity.

Because the thermal resistance of inter-tube boundaries is summed, the thermal conductivity of the bundle should be underestimated in the measurements. Based on this consideration, a simple test calculation using finite element analysis was performed. Here, a bundle was approximated as a cylindrical continuum, as illustrated in Fig. 3, which had anisotropic thermal conductivity with an anisotropy ratio of 500. The two edges of the cylindrical continuum were kept at different temperatures, T_H= 301 K and T_L= 300 K, and the heat flux passing through the center of the cylinder was probed. In the "ideal" measurement (Fig. 3a), two cross sections of the cylinder, which were located 500 nm from the center, were kept at T_H and T_L, respectively. Thus, the temperature distribution was homogeneous along the radial direction of the cylinder, and the heat flux did not depend on the radius of the cylinder. In contrast, in the "realistic" measurement (Fig. 3b), quarter sides of the cylinder's surface close to both ends were kept at T_H and T_L, respectively. In this case, heat conducted mainly along the bottom side and generated an inhomogeneous temperature distribution in the cylinder, as experimentally determined for bundled SWCNTs in this study. In addition, the heat flux decreased by increasing the radius of the cylinder.

The ratio of heat flux in the realistic case to that in ideal cases (i.e., the ratio of the apparent thermal conductivity (κ_{app}) to the intrinsic thermal conductivities (κ_{ideal})) was calculated by changing the radius of the cylinder and is plotted in Fig. 3c. Full, half, and quarter areas of the side of cylinder at both edges in the realistic case were kept at T_H and T_L. It was observed that the thermal conductivity of the bundle significantly depended on the bundle size due to the extremely high anisotropy.

The size-dependent thermal conductivity of CNT bundles has been reported in several experimental works[3,4,23] and has often been explained as the result of the suppression of some phonon modes similar to the suppression of flexural phonons of graphene on the substrate. In addition to the flexural phonons, CNTs have peculiar phonon modes, such as radial breathing mode, which also involve out-of-plane motion. Aliev *et al*. suggested such low-lying optical phonon modes are also substantially suppressed in bundles and result in low thermal conductivity of the bundle[23]. However, the radial breathing mode is detected experimentally in SWCNTs bundle by inelastic neutron scattering[22] and Raman spectroscopy, and O'Connell *et al*. reported that the bundling of SWCNTs has no significant perturbation of these frequencies[24]. Additionally, a computational study suggested that van der Waals interactions in a bundle have a negligible effect on the intrinsic conductivity of CNTs[25], which is in agreement with the small inter-tube coupling in bundles implied from the experimental data[21,24]. The effect of the extremely high anisotropy observed in this study may explain the diameter-dependent suppression of thermal conductivity of the bundled SWCNTs as shown in Fig. 3c. We can see clear changes in behavior of the curves at around 20 nm. This is due to the change of the distribution of heat flux spreading along radial direction (see Supplemental Material[20]). Below 20 nm, the curves in Fig. 3c show convex upward behaviors which is similar to the reported experimental data, rather than the model they proposed (convex downward curves)[3].

It should be noted that $\kappa_{app}/\kappa_{ideal}$ depends on the surface area kept at T_H and T_L in the realistic case, as illustrated in Fig. 3c. In the present calculation, the full, half, and quarter areas of the surface were kept at a constant temperature; however, this was likely overestimated because the contact area between the side of bundle and the membrane in the actual experiment should be very small. This would result in a steeper dependence than that displayed in Fig. 3c. To fix the specimen onto the membranes, electron- or ion-beam-assisted deposition of metals, such as platinum (Pt) and tungsten, is sometimes used in mesoscopic experiments. This may be useful to produce the contact area between the bundle and membrane; however, it would not work as a heat path. According to a previous study[26], Pt deposited in a focused ion beam apparatus contains approximately 50 at. % carbon and has considerably high electrical resistivity that is two orders of magnitude higher than that of pure Pt. Considering the Wiedemann–Franz law, thermal conductivities should decay identically.

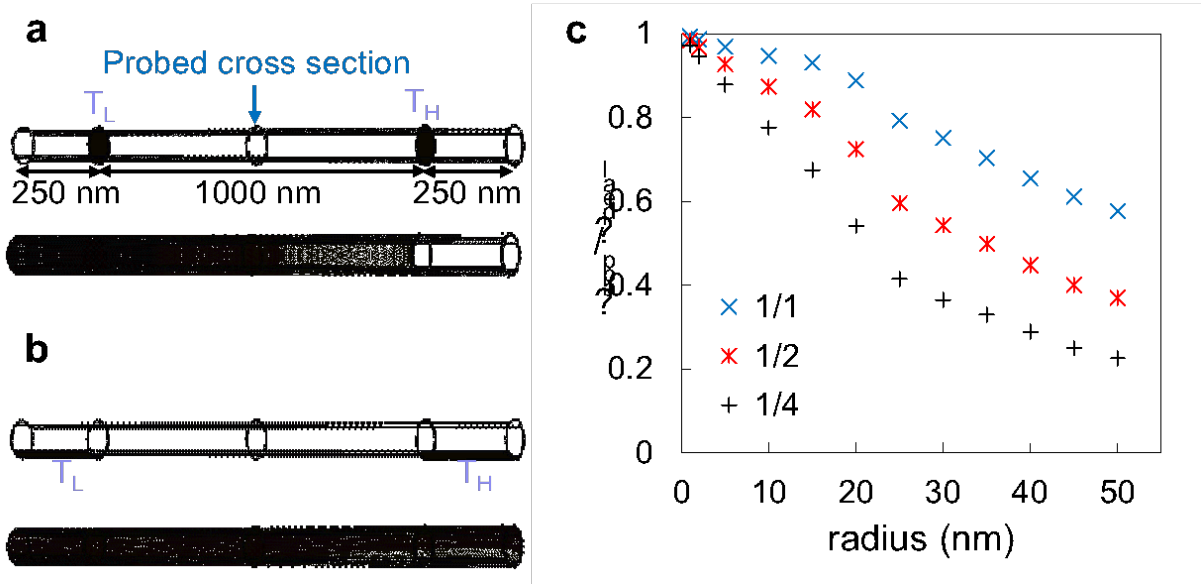


Figure 3. Finite element calculation of the ratio of the apparent thermal conductivities in realistic experimental arrangements (κ_{app}) to that in ideal arrangements (κ_{ideal}), denoted by $\kappa_{app}/\kappa_{ideal}$. (a) Calculation model of the ideal arrangement. Cross sections at two ends of the cylinder are set to different temperatures: T_H and T_L. The temperature distribution at the color scale is presented at the bottom. (b) Calculation model of realistic arrangement. Quarter of the surface at two ends of the cylinder is set to different temperatures. The temperature distribution at the color scale is presented at the bottom. (c) $\kappa_{app}/\kappa_{ideal}$ versus radius of the cylinder calculated in this model when a full, half, and quarter surface at two ends of the cylinder in the realistic case is set to T_H and T_L.

In summary, extremely high anisotropy of thermal conductivity along the directions parallel and perpendicular to the alignment of bundled SWCNTs was investigated by in situ observation of the phase transition of individual Sn nanoparticles decorating the bundle. Melting and evaporation experiments of Sn particles on the bundle revealed that the SWCNT bundle had

very high anisotropy of thermal conductivity not only at the previously reported temperature region of 1,000 °C, but also at 200 °C and 800 °C. In addition, the experiments indicated that the anisotropy increased at lower temperatures. With the aid of finite element calculation, we demonstrated that the high anisotropy estimated in this study could cause size-dependent thermal conductivity of the bundled CNTs measured in the realistic experimental arrangement. This suggests that CNT bundles have higher intrinsic thermal conductivity than the reported experimental values. Our results have important implications that may solve the discrepancy between the thermal conductivities of individual nanotubes and nanotube bundles. The proposed methodology can be used for general boundaries and is not limited to parallel boundaries in the bundle, which can help relate mesoscopic thermal behavior to macroscopic thermal behavior.

AUTHOR INFORMATION

Corresponding Author

Hiromu Hamasaki - Dept. of Mechanical Engineering, Osaka University, 2-1 Yamadaoka, Suita, Osaka, 565-0871, Japan; Email: hamasaki@ne.mech.eng.osaka-u.ac.jp

Author Contributions

All authors contributed to the discussion, interpretation, and writing the manuscript of this study. H.H. performed all experiments in the main text, analyses and simulations. T.K. partially contributed to the TEM observation and melting experiments of Sn nanoparticles. K.H. supervised the study.

Notes

The authors declare no competing interests.

ACKNOWLEDGMENT

This work was supported by JST CREST Grant Number JPMJCR17I5, Japan.

REFERENCES

1) C. Yu, L. Shi, Z. Yao, D. Li, and A. Majumdar, Thermal conductance and thermopower of an individual single-wall carbon nanotube. *Nano Lett*. **5**, 1842 (2005).

2) E. Pop, D. Mann, Q. Wang, K. Goodson, and H. Dai, Thermal conductance of an individual single-wall carbon nanotube above room temperature. *Nano Lett*. **6**, 96 (2006).

3) Y. Feng, T. Inoue, H. An, R. Xiang, S. Chiashi, and S. Maruyama, Quantitative study of bundle size effect on thermal conductivity of single-walled carbon nanotubes. *Appl*. *Phys*. *Lett*. **112**, 191904 (2018).

4) L. Shi, D. Li, C. Yu, W. Jang, D. Kim, Z. Yao, P. Kim, and A. Majumdar, Measuring thermal and thermoelectric properties of one-dimensional nanostructures using a microfabricated device. *J*. *Heat Transfer* **125**, 881 (2003).

5) T. Kodama, M. Ohnishi, W. Park, T. Shiga, J. Park, T. Shimada, H. Shinohara, J. Shiomi, and K. E. Goodson, Modulation of thermal and thermoelectric transport in individual carbon nanotubes by fullerene encapsulation. *Nat*. *Mater*. **16**, 892 (2017).

6) J. Hone, M. C. Llaguno, N. M. Nemes, A. T. Johnson, J. E. Fischer, D. A. Walters, M. J. Casavant, J. Schmidt, and R. E. Smalley, Electrical and thermal transport properties of magnetically aligned single wall carbon nanotube films. *Appl. Phys. Lett.* **77**, 666 (2000).

7) J. E. Fischer, W. Zhou, J. Vavro, M. C. Llaguno, C. Guthy, R. Haggenmueller, M. J. Casavant, D. E. Walters, and R. E. Smalley, Magnetically aligned single wall carbon nanotube films: Preferred orientation and anisotropic transport properties. *J. Appl. Phys.* **93**, 2157 (2003).

8) P. Gonnet, Z. Liang, E. S. Choi, R. S. Kadambala, C. Zhang, J. S. Brooks, B. Wang, and L. Kramer, Thermal conductivity of magnetically aligned carbon nanotube buckypapers and nanocomposites. *Curr. Appl. Phys.* **6**, 119 (2006).

9) S. Yamaguchi, I. Tsunekawa, N. Komatsu, W. Gao, T. Shiga, T. Kodama, J. Kono, and J. Shiomi, One-directional thermal transport in densely aligned single-wall carbon nanotube films. *Appl. Phys. Lett.* **115**, 223104 (2019).

10) H. Zhong, and J. R. Lukes, Interfacial thermal resistance between carbon nanotubes: Molecular dynamics simulations and analytical thermal modeling. *Phys. Rev. B* **74**, 125403 (2006).

11) S. Maruyama, Y. Igarashi, Y. Taniguchi, and J. Shiomi, Anisotropic heat transfer of single-walled carbon nanotubes. *J. Therm. Sci. Technol.* **1**, 138 (2006).

12) Y. Chalopin, S. Volz, and N. Mingo, Upper bound to the thermal conductivity of carbon nanotube pellets. *J. Appl. Phys.* **105**, 084301 (2009).

13) Z. Xu, and M. J. Buehler, Nanoengineering heat transfer performance at carbon nanotube interfaces. *ACS Nano* **3**, 2767 (2009).

14) V, Varshney, J. Lee, D. Li, J. S. Brown, B. L. Farmer, A. A. Voevodin, and A. K. Roy, Understanding thermal conductance across multi-wall carbon nanotube contacts: Role of nanotube curvature. *Carbon* **114**, 15 (2017).

15) J. Yang, S. Waltermire, Y. Chen, A. A. Zinn, T. T. Xu, and D. Li, Contact thermal resistance between individual multiwall carbon nanotubes. *Appl. Phys. Lett.* **96**, 023109 (2010).

16) H. Hamasaki, S. Takimoto, and K. Hirahara, Visualization of thermal transport within and between carbon nanotubes. *Nano Lett.* **21**, 3134 (2021).

17) T. Brintlinger, Y. Qi, K. H. Baloch, D, Goldhaber-Gordon, J. Cumings, Electron thermal microscopy. *Nano Lett.* **8**, 582 (2008).

18) C. R. M. Wronski, The size dependence of the melting point of small particles of tin. *Br. J. Appl. Phys.* **18**, 1731 (1967).

19) S. L. Lai, J. Y. Guo, V. Petrova, G. Ramanath, and L. H. Allen, Size-dependent melting properties of small tin particles: Nanocalorimetric measurements. *Phys. Rev. Lett.* **77**, 99 (1996).

20) See Supplemental Materials at for two-terminal I–V curve in heating experiment, details of finite element calculation, dark-field imaging mode of TEM for visualization of Sn melting, evaporation temperature of Sn nanoparticles, magnified TEM image, additional observations

for different bundle, power output during melting and evaporation experiment, heat source of the experiments, and heat flux along radial direction.

21) J. Hone, B. Batlogg, Z. Benes, A. T. Johnson, and J. E. Fischer, Quantized phonon spectrum of single-wall carbon nanotubes. *Science* **289**, 1730 (2000).

22) S. Rols, Z. Benes, E. Anglaret, J. L. Sauvajol, P. Papanek, J. E. Fischer, G. Coddens, H. Schober, and A. J. Dianoux, Phonon density of states of single-wall carbon nanotubes. *Phys. Rev. Lett.* **85**, 5222 (2000).

23) A. E. Aliev, M. H. Lima, E. M. Silverman, and R. H. Baughman, Thermal conductivity of multi-walled carbon nanotube sheets: radiation losses and quenching of phonon modes. *Nanotechnology* **21**, 035709 (2010).

24) M. J. O'Connell, S. Sivaram, and S. K. Doorn, Near-infrared resonance profile studies of single-walled carbon nanotube intertube interactions: A direct comparison of bundled and individually dispersed HiPco nanotubes. *Phys. Rev. B* **69**, 235415 (2004).

25) A. N. Volkov, R. N. Salaway, and L. V. Zhigilei, Atomistic simulations, mesoscopic modeling, and theoretical analysis of thermal conductivity of bundles composed of carbon nanotubes. *J. Appl. Phys.* **114**, 104301 (2013).

26) R. M. Langford, T. X. Wang, and D. Ozkaya, Reducing the resistivity of electron and ion beam assisted deposited Pt. *Microelectron. Eng.* **84**, 784 (2007).